Supersonic and Hypersonic Simulations in Three-Dimensions

EDISSON SÁVIO DE GÓES MACIEL
IEA- Aeronautical Engineering Division
ITA – Aeronautical Technological Institute
Praça Mal. Eduardo Gomes, 50 – Vila das Acácias – São José dos Campos – SP – 12228-900
BRAZIL
edissonsavio@yahoo.com.br

Abstract: - In this work, the numerical schemes of Yee, Warming and Harten, of Yee and Kutler and of Jameson and Mavriplis are implemented, according to a finite volume formulation and structured spatial discretization, to solve the Euler equations in the supersonic and hypersonic flow regimes in three-dimensions. The Yee, Warming and Harten and the Yee and Kutler schemes are of TVD flux difference splitting type, whereas the Jameson and Mavriplis scheme is a symmetrical one. All three algorithms present second order spatial accuracy. The formers are first order accurate in time, according to a time splitting method, whereas the latter is second order accurate in time, according to a Runge-Kutta method. The Jameson and Mavriplis algorithm requires still artificial dissipation to guarantee numerical stability in the presence of shock waves and backgrounds instabilities. Two models are presented: Mavriplis and Azevedo. The algorithms are applied to the steady state simulations of the supersonic flow around a simplified VLS configuration (Brazilian Satellite Launcher) and the hypersonic flows along a diffuser and an air inlet. A spatially variable time step procedure is employed to convergence accelerating. This procedure has demonstrated effective gains in convergence as reported by Maciel. The results have demonstrated the Jameson and Mavriplis algorithm, using the Mavriplis dissipation operator, as presenting the best characteristics of robustness and accuracy.

Key-Words: - Yee, Warming and Harten algorithm, Yee and Kutler algorithm, Jameson and Mavriplis algorithm, Artificial dissipation models, TVD schemes, Euler equations, Three-dimensions.

1 Introduction

The development of aerospace and aeronautical projects require hours of wind tunnel essays. It is necessary to minimize such procedures with wind tunnels due to the increasing electrical energy cost. In Brazil, there is still the problem that it has not wind tunnels of great capacity, able to generated supersonic flows or even high subsonic flows. In this way, Computational Fluid Dynamics (CFD) techniques have now great highlighted in the aerospace industry scenario. Analogue to the wind tunnels essays, the numerical methods determine the physical flow properties in discrete points of the spatial domain. Hence, the aerodynamic coefficients of lift, of drag and of momentum can be calculated.

Initially, symmetrical schemes were developed to simulate flows over simple and complex geometries due to their numerical implementation simplicity. Algorithms like predictor/corrector and symmetrical ones were the most employed during the 60's until the 80's years. Some of them are described as follows:

[1] has developed a numerical method second order accurate in space and time to solve the Navier-Stokes in two-dimensions. The algorithm was initially developed to a finite difference technique. The method was divided in two steps: one predictor and the other corrector. In the predictor step, the spatial derivatives of the flux terms were calculated with forward discretization operators and in the corrector step such derivatives were calculated with backward discretization operators.

[2] have emphasized the substantial cost reduction in the calculation of the Euler equation solutions. The method proposed by [3] had proved robustness, accuracy and sufficient sophistication to more complex applications. The objective was apply such scheme to geometries like wing-fuselage, involving rocket engines, missiles and other typical components, to represent an entire aircraft. The work emphasized the use of triangular cells, which allow a bigger flexibility in the description of complex geometries and became the mesh generation process cheaper. The fluid governing equations were discretized specially under an unstructured context. The algorithm employed a finite volume formulation with properties determined at the cell centroid. Artificial dissipation operator were constructed to guarantee second order spatial accuracy, except at the proximities of shock waves, which the accuracy was reduced to first order ([3]). A Runge-Kutta method of five stages was employed to time integration.

The need to construct more elaborate and robust algorithms, which allows the capture of strong and clear shock waves, represented an important goal to be reached by non-symmetrical schemes of first order and of high resolution. Since 1959, non-symmetrical or upwind algorithms of first and of high resolution, which combined the robustness characteristics, good shock capturing properties and good shock quality, have been developed aiming to provide efficient tools to predict the main features of the flowfield with accuracy. First order and high resolution schemes can be of flux vector splitting type or flux difference splitting type. In the former, more robust algorithms are produced, whereas in the latter bigger precision is obtained. Several studies were reported involving first order and high resolution algorithms in the international literature, as for example:

[4] have implemented an explicit method of high resolution second order accuracy, based on the [5] ideas. The method had the following properties: (a) the scheme was developed in the conservative form to assure that the limit was a weak solution; (b) the scheme satisfied an own entropy inequality to assure that the limit solution would only have physically relevant discontinuities; and (c) the scheme was designed such that a numerical dissipation yielded weak solutions highly accurate. The method was applied to the solution of a quasi one-dimensional flow along a nozzle and to the two-dimensional physical problem of a shock reflection, yielding good results. An implicit formulation was also investigated to the one- and two-dimensional cases.

[6] have presented a work that extended the [5] scheme to a generalized coordinate system, in two-dimensions. The method called "TVD scheme" by the authors was tested to the physical problem of a moving shock wave impinging a cylinder. The numerical results were compared with those of the [1] scheme, presenting good behavior.

With this scenario, an interesting and important study can be done comparing the symmetrical and upwind high resolution algorithms described herein.

The present work compares the numerical methods of [2], [4] and [6], using a finite volume formulation and a structured spatial discretization, applied to the solution of the Euler equations in three-dimensions. The aforementioned algorithms are second order accurate in space. The [2] scheme is also of second order accuracy in time and uses an artificial dissipation operator to assure convergence to the steady state solution. The [4] and [6] algorithms are first order accurate in time. The steady state physical problems of the supersonic flow around a VLS (Brazilian Satellite Launcher) simplified configuration and the hypersonic flows along a diffuser and along an air inlet are studied. A spatially variable time step procedure is implemented aiming to accelerate the convergence process. This technique has presented excellent gains in terms of convergence ratio, as reported in [7-8].

The results have demonstrated that the [2] scheme, using the [9] artificial dissipation operator, is the best algorithm in terms of robustness and accuracy characteristics.

It is important to emphasize that all algorithms presented in this work were implemented by the author, without requiring the use of commercial codes. Only the Tecplot software, version 9.0, was employed to generated the figures.

2 Euler Equations

The fluid movement is described by the Euler equations, which express the mass, the linear momentum and the energy conservations to an inviscid medium, heat non-conductor and compressible, in the absence of external forces. In the integral and conservative forms, employing a finite volume formulation and using a structured spatial discretization, to three-dimension simulations, these equations can be represented by:

$$\partial/\partial t \int_V Q dV + \int_S \left(E_e n_x + F_e n_y + G_e n_z\right) dS = 0\,, \quad (1)$$

where Q is written to a Cartesian system; V is the cell volume, which corresponds to a hexahedron in the three-dimensional space; n_x, n_y and n_z are the components of the unity vector normal to the flux face, pointing outward from the cell edge; S is the surface flux area; and E_e, F_e and G_e represent components of the convective flux vector. The determination of the hexahedral cell volume, as well its nodes and neighbors, of the components of the unity normal vector to the flux face and of the flux area are presented in [10-11]. Q, E_e, F_e and G_e are defined by:

$$Q = \begin{Bmatrix} \rho \\ \rho u \\ \rho v \\ \rho w \\ e \end{Bmatrix},\ E_e = \begin{Bmatrix} \rho u \\ \rho u^2 + p \\ \rho uv \\ \rho uw \\ (e+p)u \end{Bmatrix},\ F_e = \begin{Bmatrix} \rho v \\ \rho uv \\ \rho v^2 + p \\ \rho vw \\ (e+p)v \end{Bmatrix};\quad (2)$$

$$G_e = \begin{Bmatrix} \rho w \\ \rho uw \\ \rho vw \\ \rho w^2 + p \\ (e+p)w \end{Bmatrix}. \quad (3)$$

The quantities that appear above are described as follows: ρ is the fluid density; u, v and w are the Cartesian components of the flow velocity vector in the x, y and z directions, respectively; *e* is the total energy of the fluid per unit volume; and *p* is the static pressure of the fluid.

The Euler equations were dimensionless in relation to the freestream density, ρ_∞, and to the freestream speed of sound, a_∞, to all studied problems. To allow the solution of the matrix system of five equations to five unknowns described by Eq. (1), the state equation to a perfect gas presented below is employed.

$$p = (\gamma - 1)\left[e - 0.5\rho(u^2 + v^2 + w^2)\right], \quad (4)$$

where γ is the ratio between the specific heats at constant pressure and constant volume, respectively, which assumed the value 1.4 to the atmospheric air. The total enthalpy is determined by:

$$H = (e + p)/\rho\,. \quad (5)$$

3 [4] Algorithm

The [4] algorithm, second order accurate in space, is specified by the determination of the numerical flux vector at the (i+1/2,j,k) interface. Its extension to the interfaces (i,j+1/2,k) and (i,j,k+1/2) is straightforward, without additional complications. According to a finite volume formulation, which is equivalent to a generalized coordinate system, the volumes at the right and left flux interfaces, as also the interface volume, necessary to coordinates changes, are defined as:

$$V_R = V_{i+1,j,k},\ V_L = V_{i,j,k} \text{ and } V_{\text{int}} = 0.5(V_R + V_L), \quad (6)$$

with "*R*" and "*L*" representing right and left states of the flux interface. The flux area components at each interface are called S_{x_int}, S_{y_int} and S_{z_int} and the flux area at the interface is defined by S. All surface areas, as well the volumes aforementioned, are defined in [10-11]. The metric terms to this generalized coordinate system are defined by:

$$h_x = S_{x\_\text{int}}/V_{\text{int}},\ h_y = S_{y\_\text{int}}/V_{\text{int}},\ h_z = S_{z\_\text{int}}/V_{\text{int}}\ ; \quad (7)$$

$$h_n = S/V_{\text{int}}\,. \quad (8)$$

The properties calculated at the flux interface are obtained by arithmetical average or by Roe average ([12]). In this work, the Roe average was employed:

$$\rho_{\text{int}} = \sqrt{\rho_L \rho_R}\ ,\ u_{\text{int}} = \left(u_L + u_R\sqrt{\rho_R/\rho_L}\right)\Big/\left(1 + \sqrt{\rho_R/\rho_L}\right); \quad (9)$$

$$v_{\text{int}} = \left(v_L + v_R\sqrt{\rho_R/\rho_L}\right)\Big/\left(1 + \sqrt{\rho_R/\rho_L}\right); \quad (10)$$

$$w_{\text{int}} = \left(w_L + w_R\sqrt{\rho_R/\rho_L}\right)\Big/\left(1 + \sqrt{\rho_R/\rho_L}\right); \quad (11)$$

$$H_{\text{int}} = \left(H_L + H_R\sqrt{\rho_R/\rho_L}\right)\Big/\left(1 + \sqrt{\rho_R/\rho_L}\right); \quad (12)$$

$$a_{\text{int}} = \sqrt{(\gamma - 1)\left[H_{\text{int}} - 0.5\left(u_{\text{int}}^2 + v_{\text{int}}^2 + w_{\text{int}}^2\right)\right]}. \quad (13)$$

The eigenvalues of the Euler equations, in the ξ direction, to the convective flux are defined by:

$$U_{cont} = u_{\text{int}}h_x + v_{\text{int}}h_y\,,\ \lambda_1 = U_{cont} - a_{\text{int}}h_n\,; \quad (14)$$

$$\lambda_2 = \lambda_3 = U_{cont} \quad \text{and} \quad \lambda_4 = U_{cont} + a_{\text{int}}h_n\,. \quad (15)$$

The jumps of the conserved variables, necessary to the construction of the dissipation function of [4], are determined by:

$$\Delta\rho = V_{\text{int}}(\rho_R - \rho_L),\ \ \Delta(\rho u) = V_{\text{int}}\left[(\rho u)_R - (\rho u)_L\right]; \quad (16)$$

$$\Delta(\rho v) = V_{\text{int}}\left[(\rho v)_R - (\rho v)_L\right],\ \Delta(\rho w) = V_{\text{int}}\left[(\rho w)_R - (\rho w)_L\right]; \quad (17)$$

$$\Delta e = V_{\text{int}}(e_R - e_L). \quad (18)$$

The α vector at the (i+1/2,j,k) interface is calculated by the following expressions:

$$\left\{\alpha_{i+1/2,j,k}\right\} = \left[R^{-1}\right]_{i+1/2,j,k}\left\{\Delta_{i+1/2,j,k}Q\right\}, \quad (19)$$

with $\left[R^{-1}\right]$ defined in [10-11; 13]. The [4] dissipation function uses the right-eigenvector matrix of the normal to the flux face Jacobian matrix in generalized coordinates. This matrix is also defined in [10-11; 13].

To inviscid studies, the following entropy function is employed:

$$\nu_l = \Delta t\lambda_l = Z_l \quad \text{and} \quad \psi_l = Z_l^2 + 0{,}25\,. \quad (20)$$

Case the viscous study be accomplished, [4] suggests the following entropy function:

$$\psi_l = \begin{cases} |Z_l|, & if\ |Z_l| \geq \delta_f \\ 0.5\left(Z_l^2 + \delta_f^2\right)/\delta_f, & if\ |Z_l| < \delta_f \end{cases}, \quad (21)$$

where "*l*" varies from 1 to 5 (three-dimensional space) and δ_f assumes values between 0.1 and 0.5, being 0.2 the recommended value by [4].

The $\tilde{g}$ function at the (i+1/2,j,k) interface is defined by:

$$\tilde{g}^l = 0.5\left(\psi_l - Z_l^2\right)\alpha^l. \quad (22)$$

The g function, responsible by the artificial compressibility, is determined by:

$$g^l_{i,j,k} = signal_l \times MAX\left[0.0; MIN\left(\left|\tilde{g}^l_{i+1/2,j,k}\right|, \tilde{g}^l_{i-1/2,j,k} \times signal_l\right)\right], \quad (23)$$

where $signal_l$ is equal to 1.0 if $\tilde{g}^l_{i+1/2,j,k} \geq 0.0$ and the negative of 1.0 otherwise. The θ term, also responsible by the artificial compressibility, is defined as follows:

$$\theta^l_{i,j,k} = \begin{cases} \left|\alpha^l_{i+1/2,j,k} - \alpha^l_{i-1/2,j,k}\right| / \left(\left|\alpha^l_{i+1/2,j,k}\right| + \left|\alpha^l_{i-1/2,j,k}\right|\right), & if\ \left|\alpha^l_{i+1/2,j,k}\right| + \left|\alpha^l_{i-1/2,j,k}\right| \neq 0.0 \\ 0.0, & if\ \left|\alpha^l_{i+1/2,j,k}\right| + \left|\alpha^l_{i-1/2,j,k}\right| = 0.0 \end{cases}. \quad (24)$$

The β vector at the (i+1/2,j,k) interface is determined by the following expression:

$$\beta_l = 1.0 + \omega_l MAX\left(\theta^l_{i,j,k}, \theta^l_{i+1,j,k}\right), \quad (25)$$

in which ω_l assumes the following values: $\omega_1 = 0.25$ (non-linear field), $\omega_2 = \omega_3 = \omega_4 = 1.0$ (linear field) and $\omega_5 = 0.25$ (non-linear field). The function φ_l, velocity of numerical information transport, is defined at the interface (i+1/2,j,k) by:

$$\varphi_l = \begin{cases} \left(g^l_{i+1,j,k} - g^l_{i,j,k}\right)/\alpha^l, & if\ \alpha^l \neq 0.0 \\ 0.0, & if\ \alpha^l = 0.0 \end{cases}. \quad (26)$$

The entropy function is redefined considering φ_l and β_l: $Z_l = \nu_l + \beta_l \varphi_l$, e ψ_l is recalculated according to Eq. (20) or Eq. (21).

Finally, the [4] dissipation function, to second order accuracy in space, is constructed by the following matrix-vector product:

$$\left\{D_{YWH}\right\}_{i+1/2,j,k} = [R]_{i+1/2,j,k}\left\{\left(\beta\left(g_{i,j,k} + g_{i+1,j,k}\right) - \psi\alpha\right)/\Delta t_{i,j,k}\right\}_{i+1/2,j,k}. \quad (27)$$

The convective numerical flux vector to the interface (i+1/2,j,k) is described by:

$$F^{(l)}_{i+1/2,j,k} = \left(E^{(l)}_{\text{int}} h_x + F^{(l)}_{\text{int}} h_y + G^{(l)}_{\text{int}} h_z\right) V_{\text{int}} + 0.5 D^{(l)}_{YWH}, \quad (28)$$

with:

$$E^{(l)}_{\text{int}} = 0.5\left(E^{(l)}_R + E^{(l)}_L\right),\ F^{(l)}_{\text{int}} = 0.5\left(F^{(l)}_R + F^{(l)}_L\right); \quad (29)$$

$$G^{(l)}_{\text{int}} = 0.5\left(G^{(l)}_R + G^{(l)}_L\right). \quad (30)$$

The time integration follows the method of time splitting, first order accurate, which divides the integration in three steps, each one associated with a specific spatial direction. In the initial step, it is possible to write:

$$\Delta Q^*_{i,j,k} = -\Delta t_{i,j,k}/V_{i,j,k}\left(F^n_{i+1/2,j,k} - F^n_{i-1/2,j,k}\right);$$

$$Q^*_{i,j,k} = Q^n_{i,j,k} + \Delta Q^*_{i,j,k}; \quad (31)$$

At the intermediary step:

$$\Delta Q^{**}_{i,j,k} = -\Delta t_{i,j,k}/V_{i,j,k}\left(F^*_{i,j+1/2,k} - F^*_{i,j-1/2,k}\right);$$

$$Q^{**}_{i,j,k} = Q^*_{i,j,k} + \Delta Q^{**}_{i,j,k}; \quad (32)$$

And at the final step:

$$\Delta Q^{n+1}_{i,j,k} = -\Delta t_{i,j,k}/V_{i,j,k}\left(F^{**}_{i,j,k+1/2} - F^{**}_{i,j,k-1/2}\right);$$

$$Q^{n+1}_{i,j,k} = Q^{**}_{i,j,k} + \Delta Q^{n+1}_{i,j,k}. \quad (33)$$

4 [6] Algorithm

The [6] algorithm, second order accurate in space, follows Eqs. (6-19). The next step consists in determine the θ function, which corresponds to the artificial compression term and is responsible by the improvement of the scheme to capture more accurately discontinuities, like shock waves. One has:

$$\theta^l_{i,j} = \begin{cases} \left|\alpha^l_{i+1/2,j,k} - \alpha^l_{i-1/2,j,k}\right| \Big/ \left(\alpha^l_{i+1/2,j,k} + \alpha^l_{i-1/2,j,k}\right), & if\ \left(\alpha^l_{i+1/2,j,k} + \alpha^l_{i-1/2,j,k}\right) \neq 0.0 \\ 0.0, & if\ \left(\alpha^l_{i+1/2,j,k} + \alpha^l_{i-1/2,j,k}\right) = 0.0 \end{cases}. \quad (34)$$

The κ function at the (i+1/2,j,k) interface is defined as follows:

$$\kappa_l = 1/8\left(1 + \omega_l MAX\left(\theta^l_{i,j,k}, \theta^l_{i+1,j,k}\right)\right), \quad (35)$$

in which ω_l assumes the following values: $\omega_1 = \omega_5 = 0.25$ (non-linear fields) and $\omega_2 = \omega_3 = \omega_4 = 1.0$ (linear fields). The numerical flux function g is determined by:

$$g^l_{i,j,k} = signal_l \times MAX\left[0.0; MIN\left(\left|\alpha^l_{i+1/2,j,k}\right|, \alpha^l_{i-1/2,j,k} \times signal_l\right)\right], \quad (36)$$

where $signal_l$ assumes value 1.0 if $\alpha^l_{i+1/2,j,k} \geq 0.0$ and -1.0 otherwise. The φ_l function at the (i+1/2,j,k) interface is calculated by the following expression:

$$\varphi_l = \begin{cases} \kappa_l \left(g^l_{i+1,j,k} - g^l_{i,j,k}\right) \Big/ \alpha^l, & if\ \alpha^l \neq 0.0 \\ 0.0, & if\ \alpha^l = 0.0 \end{cases}. \quad (37)$$

The entropy function at the (i+1/2,j,k) is defined by:

$$\psi_l = \left(\nu_l + \varphi_l\right)^2 + 0.25, \quad (38)$$

with ν_l defined according to Eq. (20). Finally, the [6] dissipation function, to second order accuracy in space, is constructed by the following matrix-vector product:

$$\left\{D_{Yee/Kutler}\right\}_{i+1/2,j,k} = \left[R\right]_{i+1/2,j,k} \left\{\left(\kappa\left(g_{i,j,k} + g_{i+1,j,k}\right) - \psi\alpha\right) \Big/ \Delta t_{i,j,k}\right\}_{i+1/2,j,k}. \quad (39)$$

The Equations (28)-(30) are used to conclude the numerical flux vector of the [6] scheme and the time integration is accomplished by the time splitting method, conform described by Eqs. (31)-(33).

5 [2] Algorithm

The Equation (1) can be rewritten according to a structured spatial discretization context ([2-3]) as:

$$d\left(V_{i,j,k} Q_{i,j,k}\right) \Big/ dt + C(Q_{i,j,k}) = 0, \quad (40)$$

where:

$$\begin{aligned} C(Q_{i,j,k}) = &\left[E_e(Q_{i,j-1/2,k}) S_{x_{i,j-1/2,k}} + F_e(Q_{i,j-1/2,k}) S_{y_{i,j-1/2,k}} + G_e(Q_{i,j-1/2,k}) S_{z_{i,j-1/2,k}}\right] + \\ &\left[E_e(Q_{i+1/2,j,k}) S_{x_{i+1/2,j,k}} + F_e(Q_{i+1/2,j,k}) S_{y_{i+1/2,j,k}} + G_e(Q_{i+1/2,j,k}) S_{z_{i+1/2,j,k}}\right] + \\ &\left[E_e(Q_{i,j+1/2,k}) S_{x_{i,j+1/2,k}} + F_e(Q_{i,j+1/2,k}) S_{y_{i,j+1/2,k}} + G_e(Q_{i,j+1/2,k}) S_{z_{i,j+1/2,k}}\right] + \\ &\left[E_e(Q_{i-1/2,j,k}) S_{x_{i-1/2,j,k}} + F_e(Q_{i-1/2,j,k}) S_{y_{i-1/2,j,k}} + G_e(Q_{i-1/2,j,k}) S_{z_{i-1/2,j,k}}\right] + \\ &\left[E_e(Q_{i,j,k-1/2}) S_{x_{i,j,k-1/2}} + F_e(Q_{i,j,k-1/2}) S_{y_{i,j,k-1/2}} + G_e(Q_{i,j,k-1/2}) S_{z_{i,j,k-1/2}}\right] + \\ &\left[E_e(Q_{i,j,k+1/2}) S_{x_{i,j,k+1/2}} + F_e(Q_{i,j,k+1/2}) S_{y_{i,j,k+1/2}} + G_e(Q_{i,j,k+1/2}) S_{y_{i,j,k+1/2}}\right] \end{aligned} \quad (41)$$

is the discrete approximation of the flux integral of Eq. (1). In this work, it was adopted that, for example, the values of the primitive variables at the flux interface (i+1/2,j,k) would be obtained by arithmetical average between the values of the primitive variables at cell (i,j,k) and at cell (i+1,j,k).

The spatial discretization proposed by the authors is equivalent to a symmetrical scheme second order accurate in space, on a finite difference context. The introduction of an artificial dissipation operator is needed to guarantee the numerical stability of the algorithm in presence of, for example, uncoupled odd-even solutions and non-linear stabilities, as shock waves. Hence, Equation (40) is rewritten as:

$$d\left(V_{i,j,k} Q_{i,j,k}\right) \Big/ dt + \left[C(Q_{i,j,k}) - D(Q_{i,j,k})\right] = 0. \quad (42)$$

The time integration is performed by an explicit hybrid Runge-Kutta method of five stages, second order accurate, and can be represented in general form by:

$$\begin{aligned} Q^{(0)}_{i,j,k} &= Q^{(n)}_{i,j,k} \\ Q^{(m)}_{i,j,k} &= Q^{(0)}_{i,j,k} - \alpha_m \Delta t_{i,j,k} \Big/ V_{i,j,k} \left[C\left(Q^{(m-1)}_{i,j,k}\right) - D\left(Q^{(l)}_{i,j,k}\right)\right], \\ Q^{(n+1)}_{i,j,k} &= Q^{(m)}_{i,j,k} \end{aligned} \quad (43)$$

with $m = 1,\ldots,5$; $l = 0$ until 4; $\alpha_1 = 1/4$, $\alpha_2 = 1/6$, $\alpha_3 = 3/8$, $\alpha_4 = 1/2$ and $\alpha_5 = 1$. [2] suggest that the artificial dissipation operator should be only evaluated at the two first stages as the Euler equations were solved ($l = 0$, $m = 1$ and $l = 1$, $m =$

2). This procedure aims economy of the CPU time and also better smoothing of the numerical instabilities originated from the discretization, based on the hyperbolic characteristics of the Euler equations.

5.1 Artificial Dissipation Operator

The artificial dissipation operator implemented in [2] scheme can employs two models of weighting the different dissipation. The first one is based on the [9] work and the second one is based on the [14] study. In the present work, the two models are evaluated. The dissipation operator has the following structure:

$$D\left(Q_{i,j,k}\right)=d^{(2)}\left(Q_{i,j,k}\right)-d^{(4)}\left(Q_{i,j,k}\right), \qquad (44)$$

where:

$$\begin{aligned} d^{(2)}\left(Q_{i,j,k}\right)=\;& 0.5\varepsilon^{(2)}_{i,j-1/2,k}\left(A_{i,j,k}+A_{i,j-1,k}\right)\left(Q_{i,j-1,k}-Q_{i,j,k}\right)+\\ & 0.5\varepsilon^{(2)}_{i+1/2,j,k}\left(A_{i,j,k}+A_{i+1,j,k}\right)\left(Q_{i+1,j,k}-Q_{i,j,k}\right)+\\ & 0.5\varepsilon^{(2)}_{i,j+1/2,k}\left(A_{i,j,k}+A_{i,j+1,k}\right)\left(Q_{i,j+1,k}-Q_{i,j,k}\right)+\\ & 0.5\varepsilon^{(2)}_{i-1/2,j,k}\left(A_{i,j,k}+A_{i-1,j,k}\right)\left(Q_{i-1,j,k}-Q_{i,j,k}\right)+\\ & 0.5\varepsilon^{(2)}_{i,j,k-1/2}\left(A_{i,j,k}+A_{i,j,k-1}\right)\left(Q_{i,j,k-1}-Q_{i,j,k}\right)+\\ & 0.5\varepsilon^{(2)}_{i,j,k+1/2}\left(A_{i,j,k}+A_{i,j,k+1}\right)\left(Q_{i,j,k+1}-Q_{i,j,k}\right), \end{aligned} \qquad (45)$$

recognized as the undivided Laplacian operator and is responsible by the numerical stability in presence of shock waves; and

$$\begin{aligned} d^{(4)}\left(Q_{i,j,k}\right)=\;& 0.5\varepsilon^{(4)}_{i,j-1/2,k}\left(A_{i,j,k}+A_{i,j-1,k}\right)\left(\nabla^2 Q_{i,j-1,k}-\nabla^2 Q_{i,j,k}\right)+\\ & 0.5\varepsilon^{(4)}_{i+1/2,j,k}\left(A_{i,j,k}+A_{i+1,j,k}\right)\left(\nabla^2 Q_{i+1,j,k}-\nabla^2 Q_{i,j,k}\right)+\\ & 0.5\varepsilon^{(4)}_{i,j+1/2,k}\left(A_{i,j,k}+A_{i,j+1,k}\right)\left(\nabla^2 Q_{i,j+1,k}-\nabla^2 Q_{i,j,k}\right)+\\ & 0.5\varepsilon^{(4)}_{i-1/2,j,k}\left(A_{i,j,k}+A_{i-1,j,k}\right)\left(\nabla^2 Q_{i-1,j,k}-\nabla^2 Q_{i,j,k}\right)+\\ & 0.5\varepsilon^{(4)}_{i,j,k-1/2}\left(A_{i,j,k}+A_{i,j,k-1}\right)\left(\nabla^2 Q_{i,j,k-1}-\nabla^2 Q_{i,j,k}\right)+\\ & 0.5\varepsilon^{(4)}_{i,j,k+1/2}\left(A_{i,j,k}+A_{i,j,k+1}\right)\left(\nabla^2 Q_{i,j,k+1}-\nabla^2 Q_{i,j,k}\right), \end{aligned} \qquad (46)$$

named bi-harmonic operator, responsible by the background stability (for example, instabilities originated by the uncoupled odd-even solutions). In this last term,

$$\begin{aligned} \nabla^2 Q_{i,j,k}=\;& \left(Q_{i,j-1,k}-Q_{i,j,k}\right)+\left(Q_{i+1,j,k}-Q_{i,j,k}\right)+\left(Q_{i,j+1,k}-Q_{i,j,k}\right)+\left(Q_{i-1,j,k}-Q_{i,j,k}\right)+\\ & \left(Q_{i,j,k-1}-Q_{i,j,k}\right)+\left(Q_{i,j,k+1}-Q_{i,j,k}\right). \end{aligned} \qquad (47)$$

In the $d^{(4)}$ operator, $\nabla^2 Q_{i,j,k}$ is extrapolated from its neighbour every time that it represent a special boundary cell, recognised in the CFD literature as "ghost cell". The terms ε are defined, for instance, as:

$$\varepsilon^{(2)}_{i+1/2,j,k}=K^{(2)}MAX\ \left(\nu_{i,j,k},\nu_{i+1,j,k}\right); \qquad (48)$$

$$\varepsilon^{(4)}_{i+1/2,j,k}=MAX\ \left[0,\left(K^{(4)}-\varepsilon^{(2)}_{i+1/2,j,k}\right)\right], \qquad (49)$$

with:

$$\begin{aligned} \nu_{i,j,k}=\;& \left(\left|p_{i,j-1,k}-p_{i,j,k}\right|+\left|p_{i+1,j,k}-p_{i,j,k}\right|+\left|p_{i,j+1,k}-p_{i,j,k}\right|+\left|p_{i-1,j,k}-p_{i,j,k}\right|+\right.\\ & \left.+\left|p_{i,j,k-1}-p_{i,j,k}\right|+\left|p_{i,j,k+1}-p_{i,j,k}\right|\right)\Big/\left(p_{i,j-1,k}+p_{i+1,j,k}+p_{i,j+1,k}+\right.\\ & \left.p_{i-1,j,k}+p_{i,j,k-1}+p_{i,j,k+1}+6p_{i,j,k}\right) \end{aligned} \qquad (50)$$

representing a pressure sensor employed to identify regions of high gradients. The constants $K^{(2)}$ and $K^{(4)}$ have typical values of ¼ and 3/256, respectively. Every time that a neighbor represent a ghost cell, it is assumed that, for instance, $\nu_{ghost}=\nu_{i,j,k}$. The $A_{i,j,k}$ terms define the weighting coefficients of the dissipation. Two models are studied: [9] and [14].

5.1.1 Dissipation Coefficient – [9] Model

The $A_{i,j,k}$ terms represent contributions from the maximum normal eigenvalue of the Euler equations integrated around each cell face. This term is defined by:

$$\begin{aligned} A_{i,j,k}=\;& \left\{\left|0.5\left(u_{i,j,k}+u_{i,j-1,k}\right)S_{x_{i,j-1/2,k}}+0.5\left(v_{i,j,k}+v_{i,j-1,k}\right)S_{y_{i,j-1/2,k}}+\right.\right.\\ & \left.0.5\left(w_{i,j,k}+w_{i,j-1,k}\right)S_{z_{i,j-1/2,k}}\right|+0.5\left(a_{i,j,k}+a_{i,j-1,k}\right)\left(S^2_{x_{i,j-1/2,k}}+S^2_{y_{i,j-1/2,k}}+S^2_{z_{i,j-1/2,k}}\right)^{0.5}\Big]+\\ & \Big[\left|0.5\left(u_{i,j,k}+u_{i+1,j,k}\right)S_{x_{i+1/2,j,k}}+0.5\left(v_{i,j,k}+v_{i+1,j,k}\right)S_{y_{i+1/2,j,k}}+0.5\left(w_{i,j,k}+w_{i+1,j,k}\right)S_{z_{i+1/2,j,k}}\right|+\\ & \left.0.5\left(a_{i,j,k}+a_{i+1,j,k}\right)\left(S^2_{x_{i+1/2,j,k}}+S^2_{y_{i+1/2,j,k}}+S^2_{z_{i+1/2,j,k}}\right)^{0.5}\right]+ \end{aligned}$$

$$\left|0.5\left(u_{i,j,k}+u_{i,j+1,k}\right)S_{x_{i,j+1/2,k}}+0.5\left(v_{i,j,k}+v_{i,j+1,k}\right)S_{y_{i,j+1/2,k}}+0.5\left(w_{i,j,k}+w_{i,j+1,k}\right)S_{z_{i,j+1/2,k}}\right|+$$
$$0.5\left(a_{i,j,k}+a_{i,j+1,k}\right)\left(S^2_{x_{i,j+1/2,k}}+S^2_{y_{i,j+1/2,k}}+S^2_{z_{i,j+1/2,k}}\right)^{0.5}\Big]+$$
$$\left|0.5\left(u_{i,j,k}+u_{i-1,j,k}\right)S_{x_{i-1/2,j,k}}+0.5\left(v_{i,j,k}+v_{i-1,j,k}\right)S_{y_{i-1/2,j,k}}+0.5\left(w_{i,j,k}+w_{i-1,j,k}\right)S_{z_{i-1/2,j,k}}\right|+$$
$$0.5\left(a_{i,j,k}+a_{i-1,j,k}\right)\left(S^2_{x_{i-1/2,j,k}}+S^2_{y_{i-1/2,j,k}}+S^2_{z_{i-1/2,j,k}}\right)^{0.5}\Big]+$$
$$\left|0.5\left(u_{i,j,k}+u_{i,j,k-1}\right)S_{x_{i,j,k-1/2}}+0.5\left(v_{i,j,k}+v_{i,j,k-1}\right)S_{y_{i,j,k-1/2}}+0.5\left(w_{i,j,k}+w_{i,j,k-1}\right)S_{z_{i,j,k-1/2}}\right|+$$
$$0.5\left(a_{i,j,k}+a_{i,j,k-1}\right)\left(S^2_{x_{i,j,,k-/2}}+S^2_{y_{i,j,k-1/2}}+S^2_{z_{i,j,k-1/2}}\right)^{0.5}\Big]+$$
$$\left|0.5\left(u_{i,j,k}+u_{i,j,k+1}\right)S_{x_{i,j,k+1/2}}+0.5\left(v_{i,j,k}+v_{i,j,k+1}\right)S_{y_{i,j,k+1/2}}+0.5\left(w_{i,j,k}+w_{i,j,k+1}\right)S_{z_{i,j,k+1/2}}\right|+$$
$$0.5\left(a_{i,j,k}+a_{i,j,k+1}\right)\left(S^2_{x_{i,j,,k+/2}}+S^2_{y_{i,j,k+1/2}}+S^2_{z_{i,j,k+1/2}}\right)^{0.5}\Big], \quad (51)$$

with "*a*" representing the speed of sound.

5.1.2 Dissipation Coefficient – [14] Model

The $A_{i,j,k}$ terms represent dissipation coefficients with the required properties to weighting:

$$A_{i,j,k}=V_{i,j,k}/\Delta t_{i,j,k}\,. \quad (52)$$

(i) Smaller time steps, bigger dissipation;

(ii) Bigger cells, bigger dissipation.

6 Spatially Variable Time Step

To steady state problems, the spatially variable time step procedure is employed to each hexahedron (i,j,k) aiming to accelerate the convergence process. The idea of the spatially variable time step procedure is keeping a constant CFL number in the whole calculation domain and, with it, guarantees time steps appropriated for each mesh region during the convergence process. The spatially variable time step can be defined as:

$$\Delta t_{i,j,k}=CFL\left(\Delta s\right)_{i,j,k}/\left(\left|q\right|+a\right)_{i,j,k}\,, \quad (53)$$

where CFL is the Courant-Friedrichs-Lewis number that provides stability to the method; $\left(\Delta s\right)_{i,j,k}$ is a characteristic length of information transport; and $\left(\left|q\right|+a\right)_{i,j,k}$ is the maximum characteristic velocity of information transport, which "*a*" is the speed of sound. The characteristic length of information transport, $\left(\Delta s\right)_{i,j,k}$, can be determined by:

$$\left(\Delta s\right)_{i,j,k}=\left[MIN\left(l_{MIN},C_{MIN}\right)\right]_{i,j,k}, \quad (54)$$

with l_{MIN} being the minimum side length that composes a computational cell and C_{MIN} is the minimum baricenter distance between the computational cell and its neighbors. The maximum characteristic velocity of information transport is defined by $\left(\left|q\right|+a\right)_{i,j,k}$, with $q=\sqrt{u^2+v^2+w^2}$.

7 Initial and Boundary Conditions

7.1 Initial Conditions

The initial condition adopted for all problems is the freestream flow in the whole calculation domain ([2] and [15]). The vector of conserved variables is expressed as follows:

$$Q_\infty=\left\{1 \quad M_\infty\cos\theta \quad M_\infty sen\theta\cos\psi \quad M_\infty sen\theta sen\psi \quad \left[\frac{1}{\gamma(\gamma-1)}+\frac{M_\infty^2}{2}\right]\right\}^t \quad (55)$$

where M_∞ represents the freestream Mach number, θ is the upstream incidence angle of the flow in relation to the configuration under analysis and ψ is the angle at the longitudinal configuration plane.

7.2 Boundary Conditions

The different types of boundary conditions implemented in this work are described below.

(a) Wall – The Euler case requires the flux tangency condition. Under the finite volume context, this imposition is done considering that the velocity component tangent to the wall ghost cell be equal to the corresponding velocity component tangent to the wall neighbor real cell. At the same time, the velocity component normal to the wall ghost cell should be equal to the negative of the velocity component normal to the wall of its neighbor real cell. The pressure gradient in which the fluid is submitted in the normal direction to the wall is equal to zero. The temperature gradient is also equal to zero along the entire wall. With these assumptions, the pressure, temperature and density are obtained from zero order extrapolation. The total energy is obtained by the perfect gas state equation.

(b) Far field – In the implementation of the boundary conditions at the external region of the

mesh domain to physical problems of external flow, it is important to differentiate four possible physical situations: entrance with subsonic flow, entrance with supersonic flow, exit with subsonic flow and exit with supersonic flow. In the present study, considering that the unique problem of external flow is supersonic, only will exist the supersonic entrance and exit conditions.

(b.1) Entrance with supersonic flow – All variables are specified at the entrance boundary of the calculation domain in terms of the freestream flow values;

(b.2) Exit with supersonic flow – The five characteristics which command the Euler equations goes from the internal region of the calculation domain, not being possible to specify values of the exit variables. Zero order extrapolation is applied to density, velocity components and pressure.

(c) Entrance and Exit – The entrance and exit boundaries are applied to the internal flow problems. Boundary conditions which involve flow entrance at the computational domain had the flow properties fixed as values of freestream flow. Boundary conditions which involve exit of the computational domain used simply the zero order extrapolation. These conditions are valid because the studied flows are no minimal supersonic in the entrance and exit boundaries.

(d) Continuity Condition – In the VLS problem, there is the continuity of the flow in the longitudinal section that passing by the configuration center. This requires that the vector of conserved variables be the same at the upper and lower regions of the symmetry plane.

8 Results

Tests were performed on a notebook with processor INTEL PENTIUM DUAL CORE with 2.3GHz of "clock" and 3.0GBytes of RAM. The convergence criterion adopted for obtaining the steady state solutions was the reduction of four (4) orders of magnitude in the value of maximum residual in the field, a typical criterion in the CFD community. The maximum residual in the field was defined as the biggest value obtained from the five (5) discretized equations.

Three physical problems were studied: the supersonic flow around a simplified version of the VLS, the hypersonic flow along a diffuser and the hypersonic flow along an air inlet.

The flow attack angle and the longitudinal plane angle were considered equals to zero in the present study. The wall pressure distributions were obtained in the configuration longitudinal plane to the VLS case and in the planes k = KMAX/2, in which KMAX is the maximum number of points in the z direction, to the diffuser and air inlet cases. To the calculation of the shock angle in the diffuser and air inlet problems, it was considered pressure contours at the xy plane of these geometries.

8.1 VLS Problem

The first problem under study consists in the simulation of the supersonic flow around a simplified configuration of the VLS. Such configuration is described in Fig. 1. Figure 2 exhibits the three-dimensional mesh generated to this configuration. It is composed of 65x50x40 points, which is equivalent in finite volumes to be formed by 147,264 hexahedral cells and 156,000 nodes.

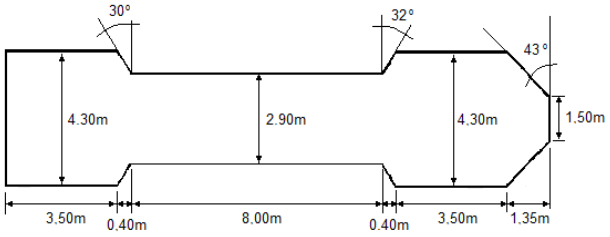

Figure 1. Geometry of the VLS configuration.

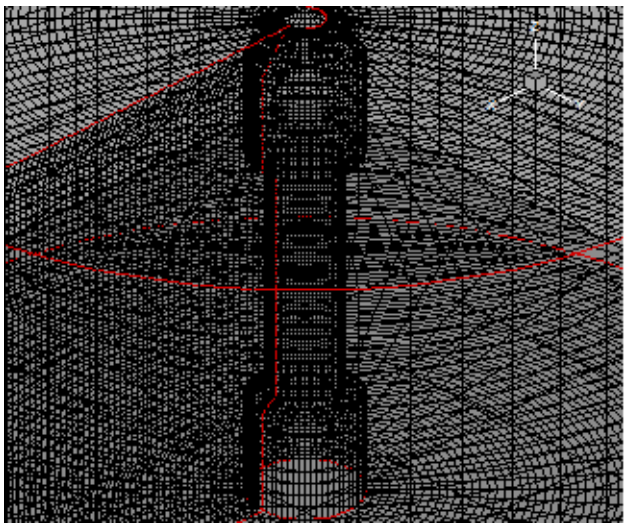

Figure 2. Mesh to the VLS configuration.

The initial condition adopted a freestream Mach number of 4.0, which represents one of VLS flight phases. Figures 3 to 6 exhibit the pressure contours obtained by the [4], [6] and [2] schemes, respectively. The [2] scheme presents two solutions due to the two dissipation models studied in this work ([9] and [14]). As can be observed, the [4] and

[6] solutions do not present good symmetry properties and homogeneity of the pressure contours. It is also possible to observe that the [4] solution presents a small pressure oscillation at the boosters region. In the region of the satellite transport compartment is also possible observe oscillations in the maximum pressure, proportionating a non-homogenous region in the [6] solution.

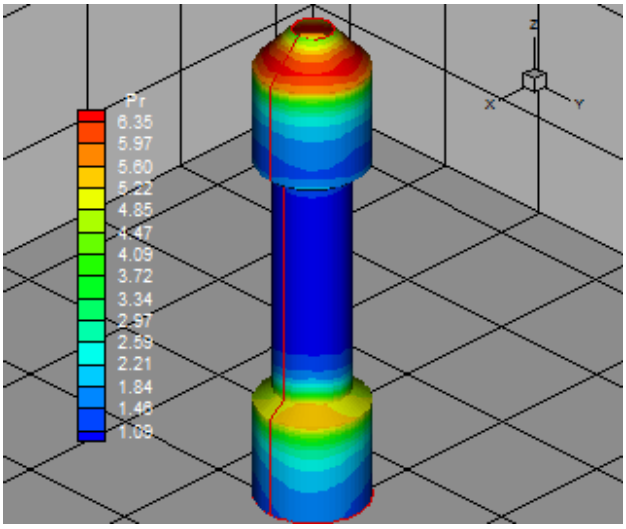

Figure 3. Pressure contours ([4]).

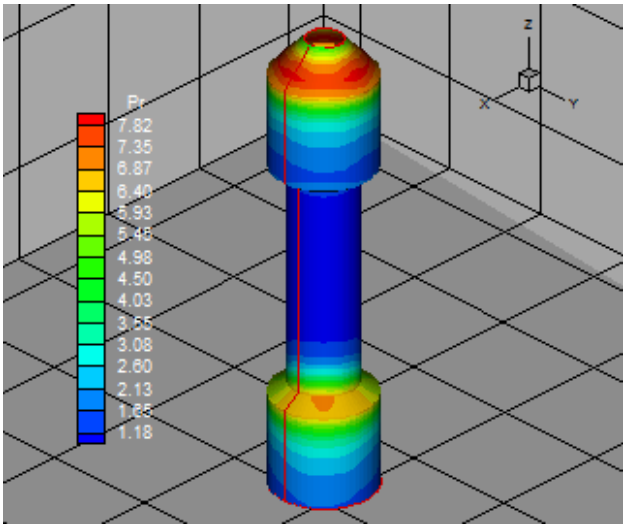

Figure 4. Pressure contours ([6]).

In [4], the solution presents the same problem of non-homogeneity in the pressure field at the satellite region. With relation to the [2] solutions, it is possible to observe homogeneity in the pressure distribution along the configuration. The most critical region, the charge compartment, is free of oscillations. Both solutions of [2] only present meaningful differences in the central region of the VLS, at the end of the charge compartment. There is a pressure reduction bigger in the region detected by the [2] scheme with the [14] dissipation operator than with the [9] dissipation operator. This more severe pressure reduction is noted mainly in the [4] and [6] solutions. The [2] behavior with the [9] dissipation operator is smoother, only having a more severe pressure loss at the end of the boosters region. It is also possible to note that the pressure peak at the satellite compartment is bigger in the [2] solutions than in the [4] and [6] solutions.

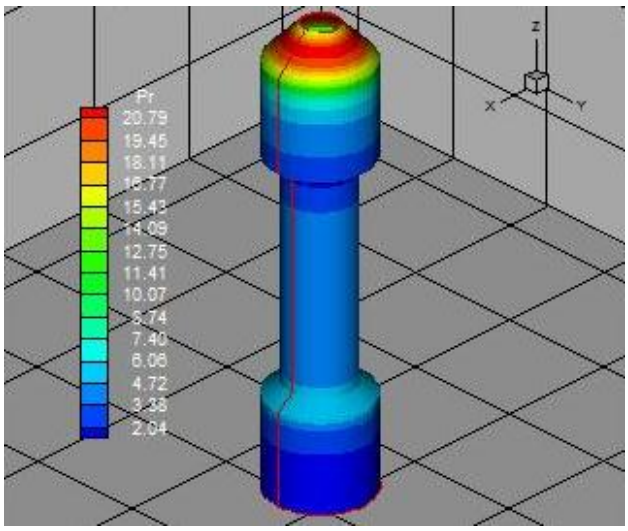

Figure 5. Pressure contours ([2] and [9]).

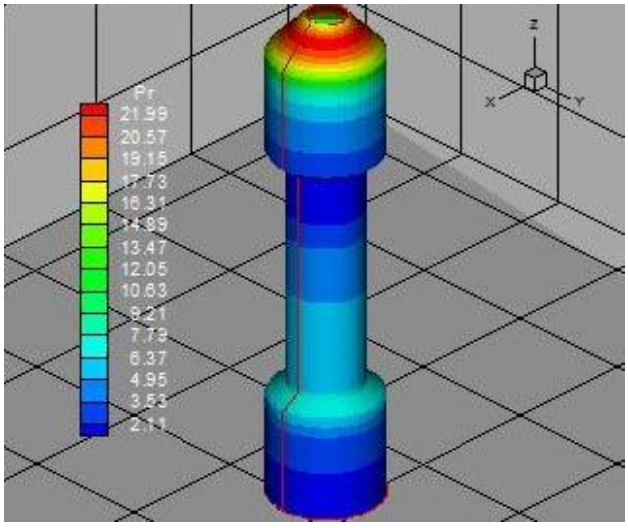

Figure 6. Pressure contours ([2] and [14]).

Figures 7 to 10 exhibit the Mach number contours obtained by [4], [6] and [2]. As can be observed, there is a bigger reduction in the value of the Mach number at the charge region in the solutions generated by [4] and [6] than in the [2] solutions. However, the recovery of the Mach number is more intense in the [4] and [6] solutions,

as observed at the cylindrical region in the charge compartment.

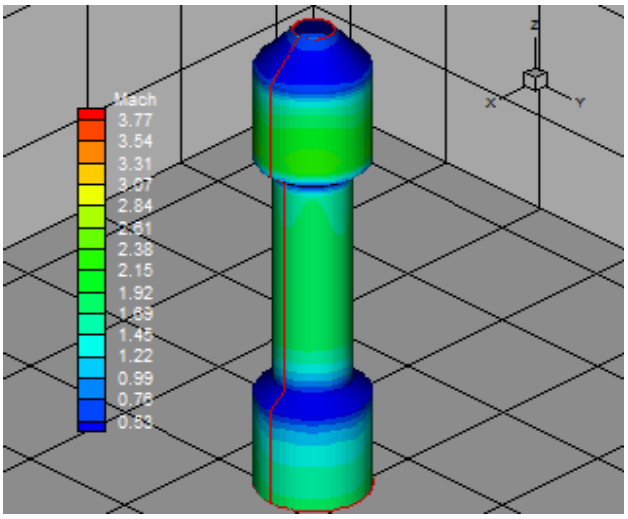

Figure 7. Mach number contours ([4]).

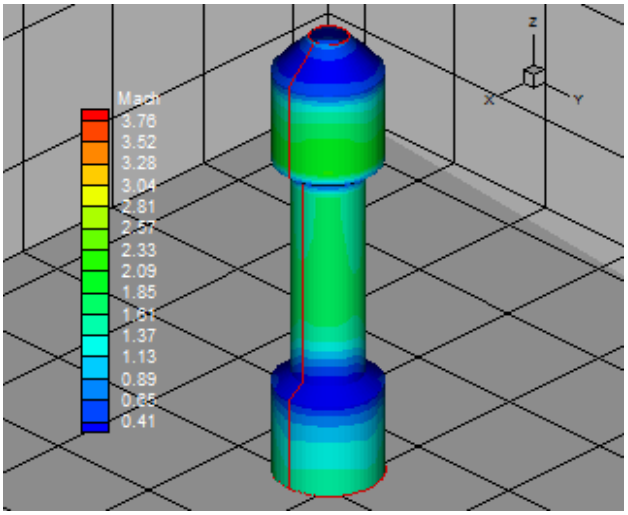

Figure 8. Mach number contours ([6]).

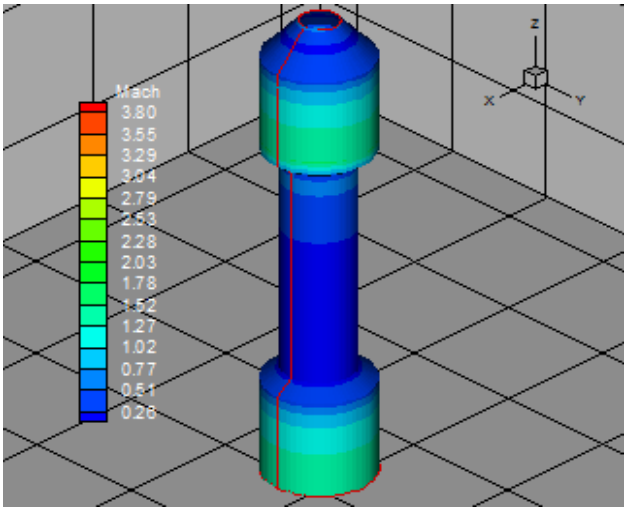

Figure 9. Mach number contours ([2] and [9]).

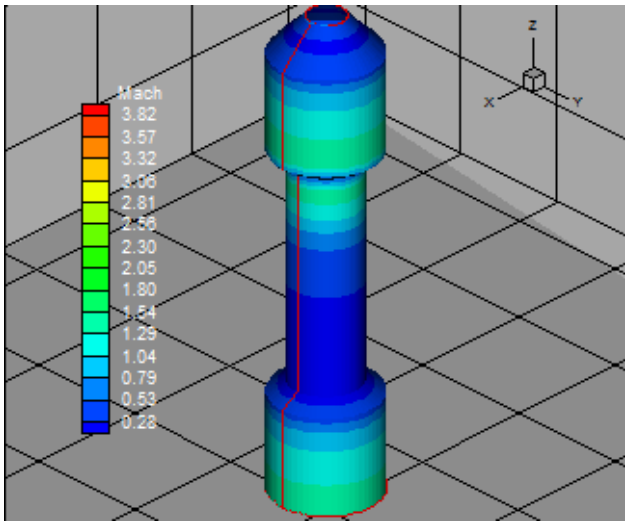

Figure 10. Mach number contours ([2] and [14]).

Figures 11 to 14 present the temperature contours due to translation and rotation obtained by [4], [6] and [2]. It is possible to note that there are temperature oscillations at the charge compartment in the solutions obtained by [4] and [6]. The [2] solutions are more homogeneous. An interesting feature is that the [4] and [6] solutions present temperature increase at the boosters region, due to the geometry and to the second shock, what should also be captured by the [2] algorithms.

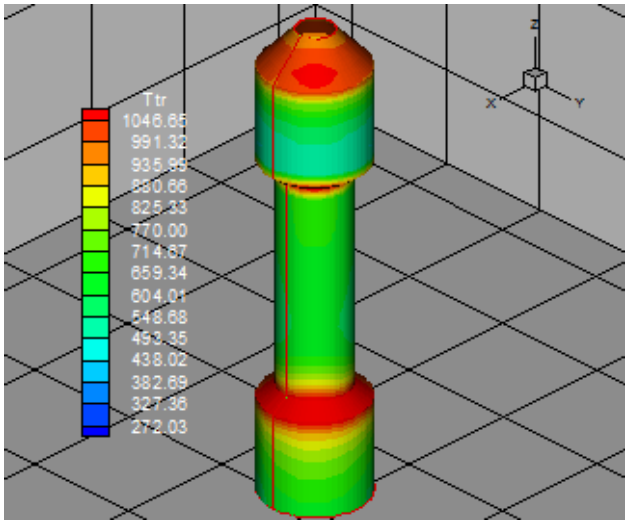

Figure 11. Temperature contours ([4]).

Figure 15 exhibits the –Cp distributions obtained by the [4], [6] and [2] schemes, along the VLS wall, in the z direction. It is possible to observe that all schemes capture the two shock at the ramp of the charge compartment and at the ramp representative of the boosters region. At the VLS body, the pressure is maintained constant and this behavior is mainly observed in the [4] and [6] solutions. At the

second shock, the maximum pressure is obtained by the [6] and [2] schemes using the [14] dissipation operator. The pressure is smoothed by the expansion fan at the boosters region. As can be observed, the best qualitative behavior, in relation to the pressure distribution, is obtained by [4] and [6].

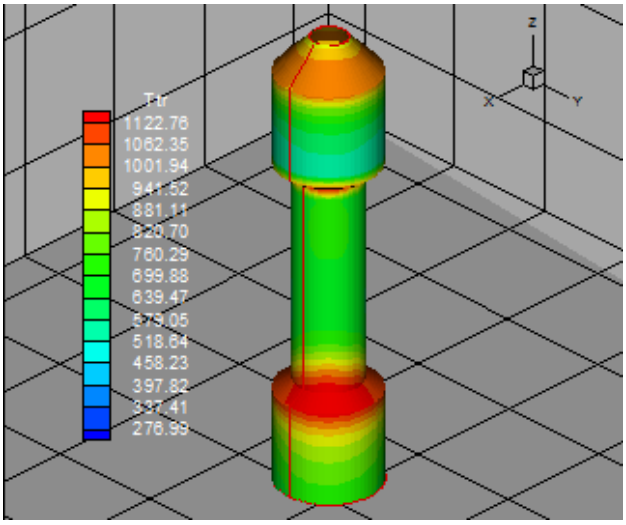

Figure 12. Temperature contours ([6]).

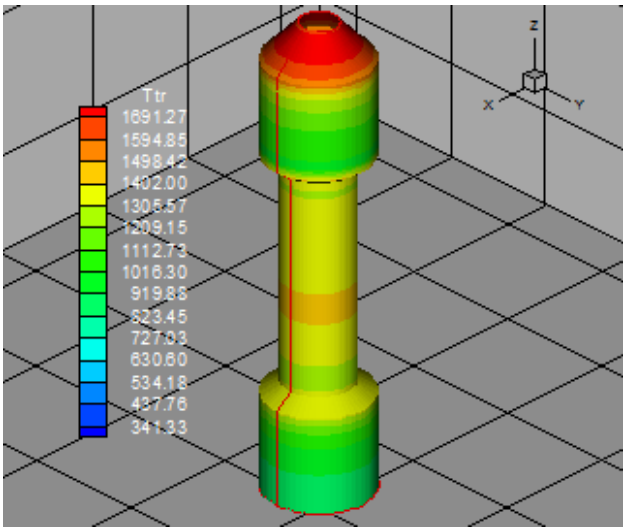

Figure 13. Temperature contours ([2] and [9]).

A possibility of quantitative comparison of all schemes is the determination of the stagnation pressure ahead of the configuration. [16] presents a table with normal shock wave properties in its B Appendix. This table allows the determination of some shock wave properties as function of the freestream Mach number. Ahead of the VLS configuration studied in this work, the shock wave presents a normal shock wave behavior, which allows the determination of the stagnation pressure, behind the shock wave, from the tables encountered in [16]. Hence, it is possible to determine the ratio pr_0/pr_∞ from [16], where pr_0 is the stagnation pressure ahead of the configuration and pr_∞ is the freestream flow pressure (equal to $1/\gamma$ to the present dimensionless of the problem).

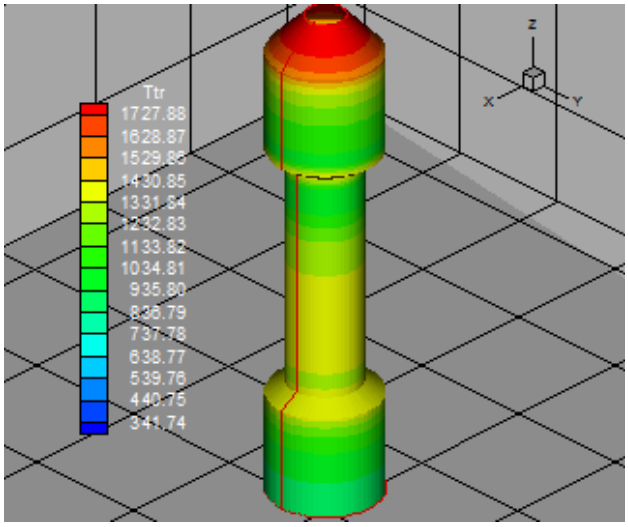

Figure 14. Temperature contours ([2] and [14]).

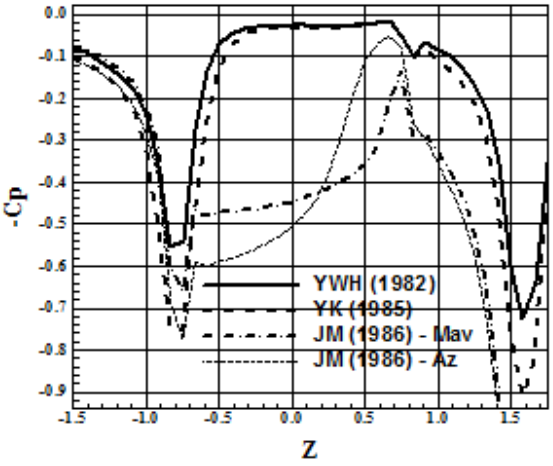

Figure 15. –Cp distributions.

Hence, to this problem, $M_\infty = 4.0$ corresponds to $pr_0/pr_\infty = 21.07$ and remembering that $pr_\infty = 0.714$, is possible to conclude that $pr_0 = 15.05$. Values of the stagnation pressure and percentage errors, respectively, are described in Tab. 1.

Table 1. Values of stagnation pressure to the VLS problem.

Algorithm	pr_0	Error (%)
[4]	6.35	57.81
[6]	7.82	48.04
[2] and [9]	20.79	38.14
[2] and [14]	21.99	46.11

The results indicate that the symmetrical scheme [2], using the dissipation operator [9], is the one that

present the closest value to the theoretical prediction of the stagnation pressure, with a percentage error of 38.14%, considered as a reasonable solution.

8.2 Diffuser Problem

The diffuser configuration is presented in Fig. 16. Its width is of 0.10m. Its mesh is composed of 61x61x10 points, or, equivalently, to 32,400 hexahedral cells and 37,210 nodes. The freestream Mach number to this simulation was adopted equal to 10.0, characterizing a hypersonic flow regime. The main characteristic of this problem is the formation of two shock waves at the upper and lower walls of the diffuser and the interception of them at the throat.

Figure 17 exhibit the mesh to this diffuser configuration. It is equally spaced in x and y directions because the Euler equations are solved.

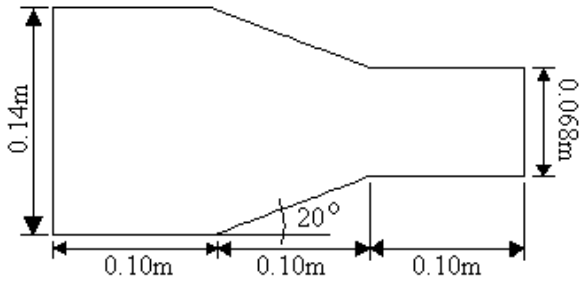

Figure 16. Diffuser configuration geometry.

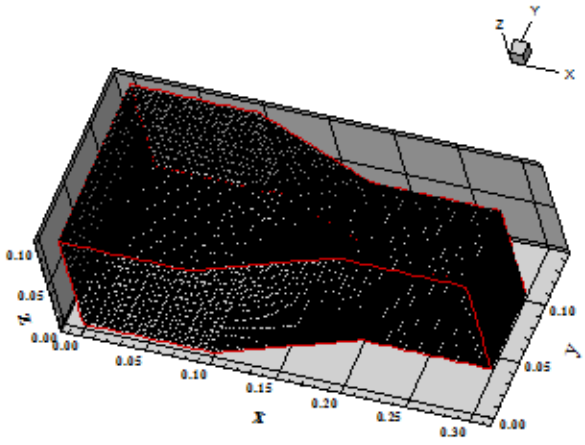

Figure 17. Mesh to the diffuser configuration.

Figures 18 to 21 show the pressure contours obtained by [4], [6] and [2] to the diffuser problem. The two shock waves are well captured by the four (4) numerical algorithms. The pressure peak, at the intersection region, has a value of approximately 50.13 in the most severe case obtained by the [2] algorithm with the [14] dissipation operator. The [2] scheme presents more homogeneous solutions in its two variants.

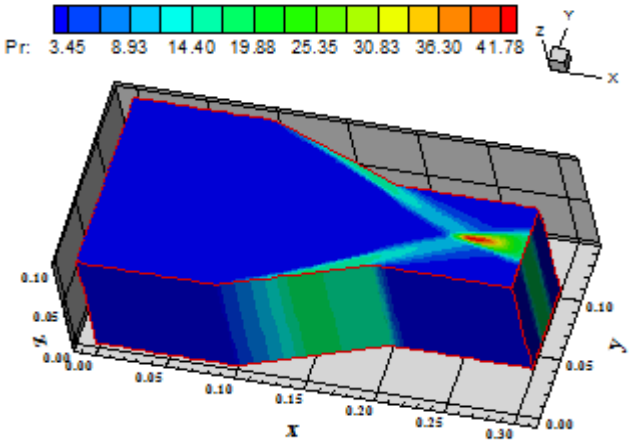

Figure 18. Pressure contours ([4]).

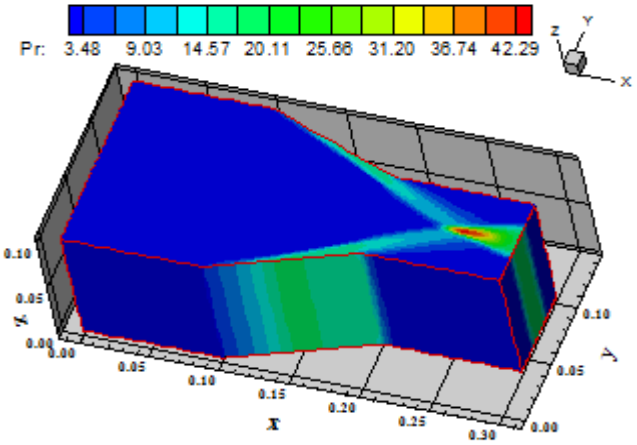

Figure 19. Pressure contours ([6]).

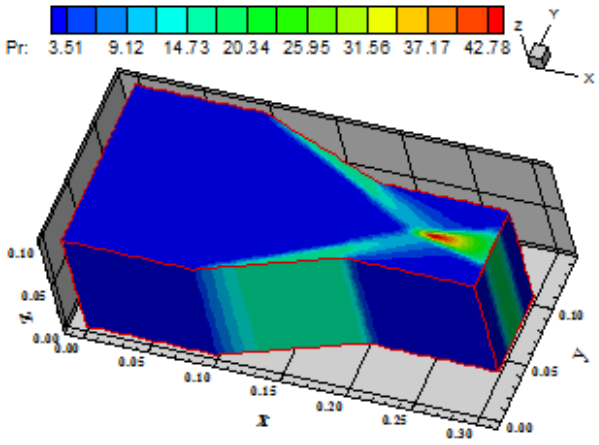

Figure 20. Pressure contours ([2] and [9]).

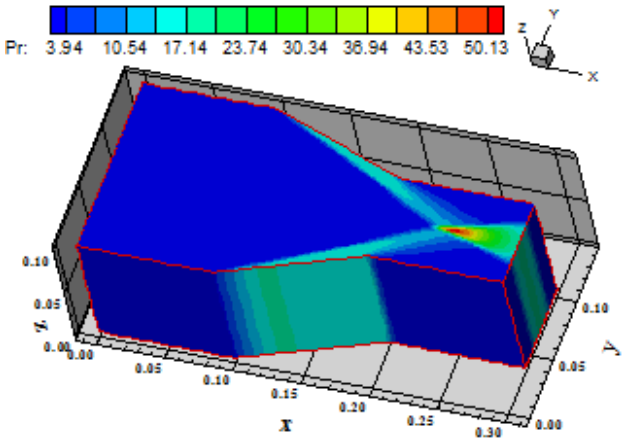

Figure 21. Pressure contours ([2] and [14]).

Figures 22 to 25 present the Mach number contours along the diffuser obtained by the four (4) numerical schemes. The Mach number peak is obtained by [2] employing the [14] dissipation operator. The shock wave intersection is well captured by all schemes and the solution tri-dimensionality is verified.

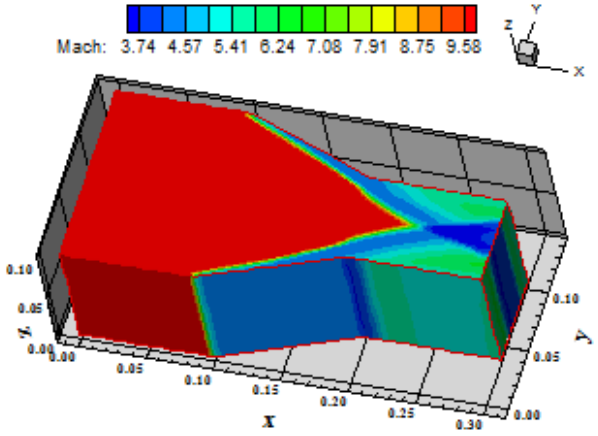

Figure 22. Mach number contours ([4]).

Figures 26 to 29 show the temperature contours obtained from the solutions of the [4], [6] and [2] schemes. All solutions capture the main features of the flow and the shock intersection. The temperature peak at the intersection is obtained by [2] using the dissipation operator [14]. All schemes detect a small increase in the temperature at the diffuser-ramp end, which can be due to the rarefied flow (expansion fan) that happens at this region. The shock waves are well captured conform aforementioned.

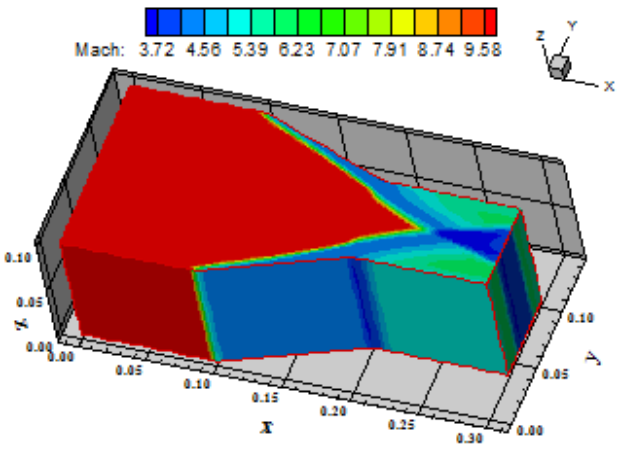

Figure 23. Mach number contours ([6]).

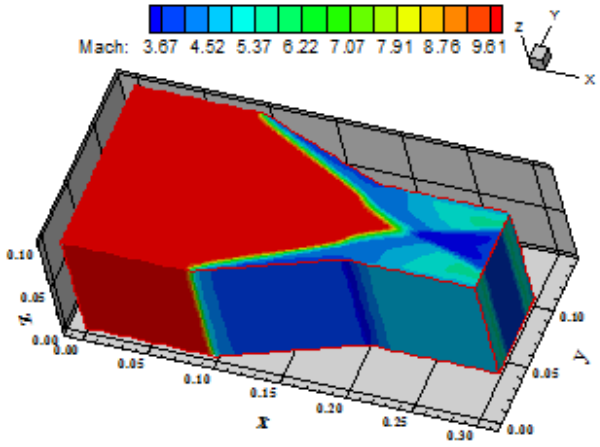

Figure 24. Mach number contours ([2] and [9]).

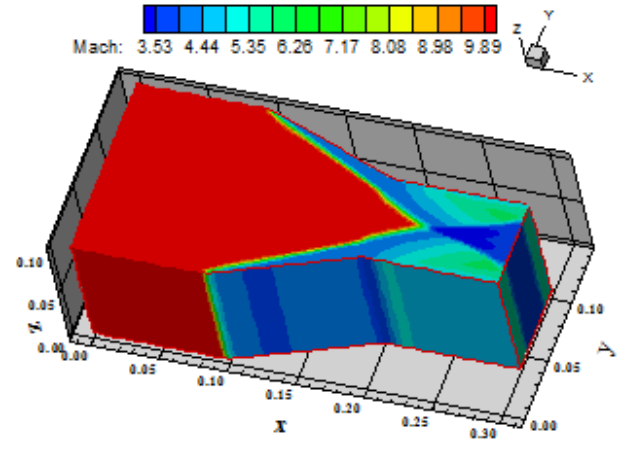

Figure 25. Mach number contours ([2] and [14]).

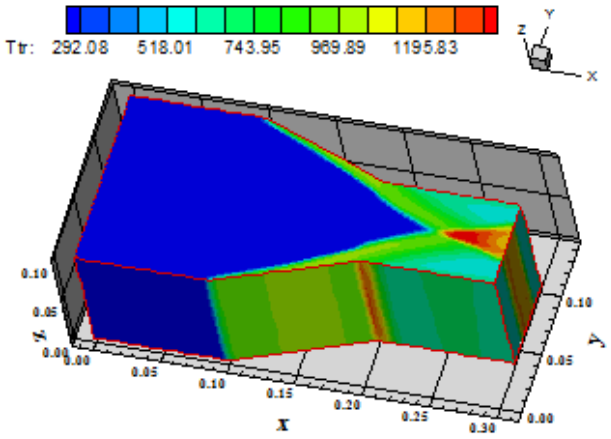

Figure 26. Temperature contours ([4]).

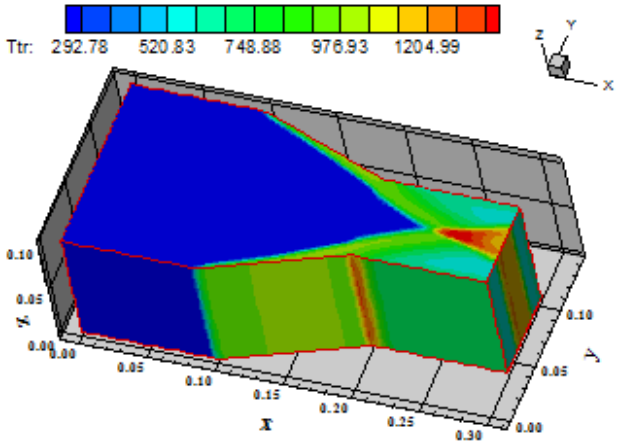

Figure 27. Temperature contours ([6]).

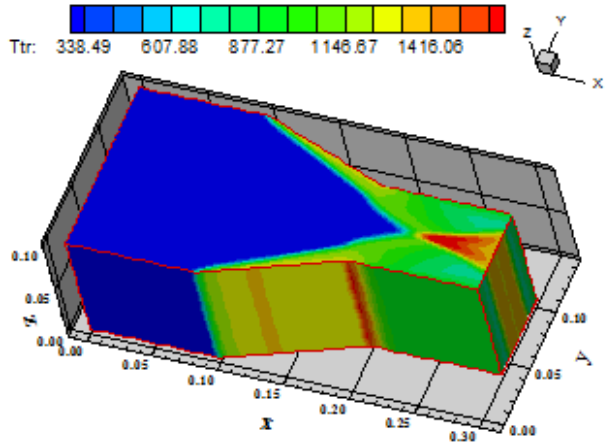

Figure 28. Temperature contours ([2] and [9]).

Figure 30 presents the pressure distributions at the diffuser inferior wall obtained by the numerical schemes of [4], [6] and [2]. They are compared with the theoretical results of the oblique shock wave and the Prandtl-Meyer expansion fan.

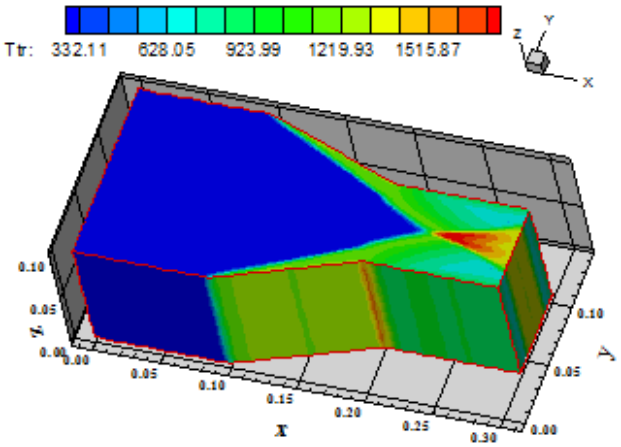

Figure 29. Temperature contours ([2] and [14]).

As can be seen, all solutions present oscillations at the shock plateau, being the smoothest that obtained by [2], employing the [9] dissipation operator. All solutions capture well the pressure value after the expansion fan (flow recovery pressure). The plateau width is best estimated by the [2] scheme using the [14] dissipation operator.

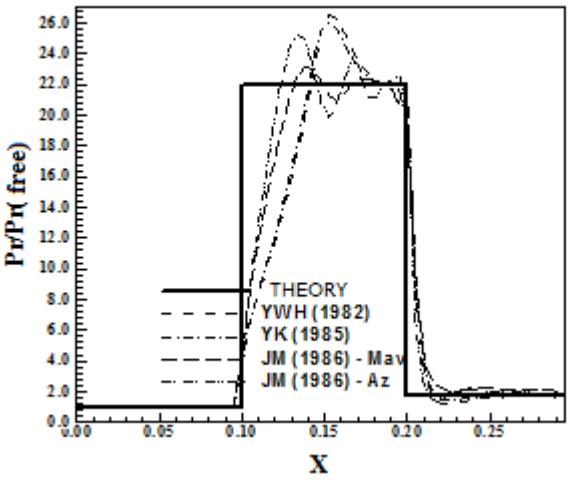

Figure 30. Pressure distributions at the inferior wall.

A way to verify quantitatively if the solutions generated by the [4], [6] and [2] are satisfactory consists in determine the shock angle of the oblique shock wave, β, measured in relation to the initial direction of the flowfield. [16] (pages 352 and 353) presents a diagram with values of the shock angle, β, to oblique shock waves. The value of this angle is determined as function of the freestream Mach number and the flow deflection angle behind the shock wave, ϕ .To $\phi = 20^{o}$ (diffuser inclination angle)

and to a freestream Mach number equal to 10.0, it is possible to obtain from this diagram a value to β equal to 26.0°. Employing a transfer in Figs. 18 to 21, at the xy plane, it is possible to obtain the values of β to each scheme, as also the respective percentage errors, exhibited in Tab. 2. The [2] scheme with the [9] dissipation operator was the best algorithm, yielding the best results to the shock angles of the lower and upper walls.

Table 2. Values of the shock angles and percentage errors to the diffuser problem.

Scheme	β (lower)	Error (%)	β(Upper)	Error (%)
[4]	23.9	8.08	25.6	1.54
[6]	25.4	2.31	25.0	3.85
[2]-[9]	26.0	0.00	25.9	0.38
[2]-[14]	25.9	0.38	25.9	0.38

8.3 Air Inlet Problem

Figure 31 exhibits the air inlet configuration employed in these studies. Its lengths are given in millimeters. The dashed region ahead of the entrance boundary is to allow that the flow enters the device parallel to the x direction and suffers less impact due to the ramps. Ghost volumes are employed in this region to assure the properties of flow entrance and the tangency in relation to the horizontal.

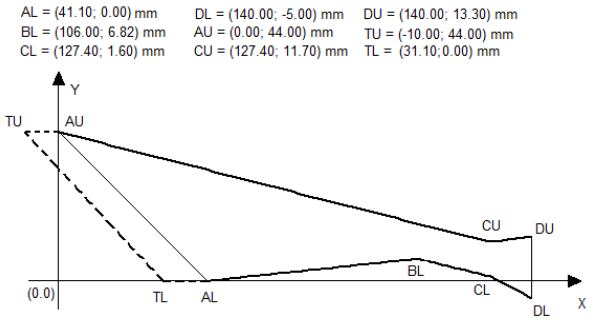

Figure 31. Air inlet configuration geometry.

Figure 32 presents the computational mesh employed in the simulations. The mesh has 60x40x15 points in a finite difference context or is composed of 32,214 hexahedral cells and 36,000 nodes. This mesh does not have any stretching, being equally spaced in all three dimensions. This mesh was algebraically generated, with the configuration constructed in the xy plane and after that repeated in the parallel z planes.

In the simulations, only the [2] scheme generated converged results with the dissipation operators [9] and [14]. The other schemes [4] and [6] were not sufficiently robust to support the problem initial condition.

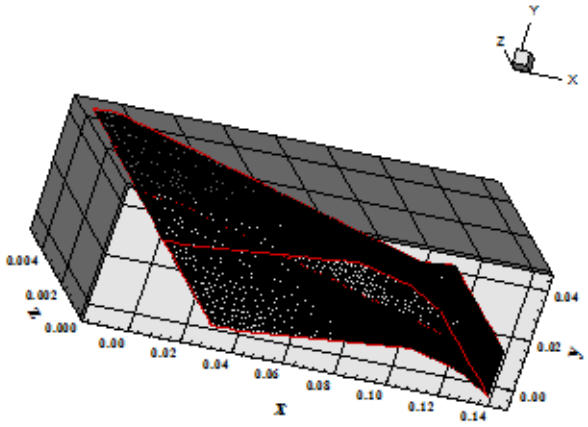

Figure 32. Air inlet configuration mesh.

The initial condition adopted a freestream Mach number equal to 15.0, which represents a high hypersonic flow and more severe than the others, being the most representative of the possibilities of a scheme demonstrate its robustness and accuracy.

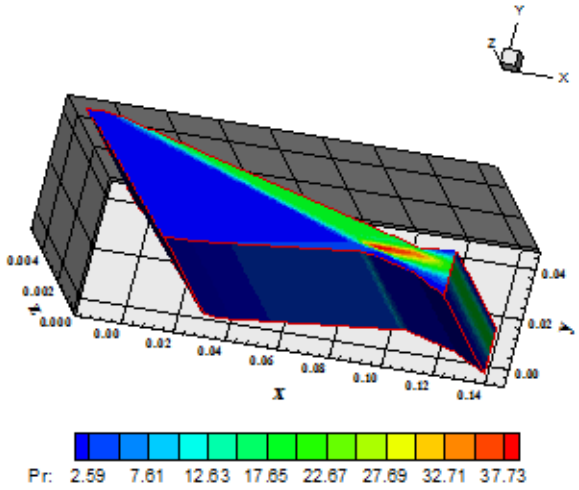

Figure 33. Pressure contours ([2] and [9]).

Figures 33 and 34 show the pressure contours obtained by [2] using the [9] and [14] dissipation operators, respectively. As can be seen, the most severe pressure field is due to [2] using the artificial dissipation operator of [9]. Both solutions present qualitative differences in relation to the shock wave thickness at the lower and upper air inlet walls. The oblique shock waves are less thicken in the solution generated by [2] with the [9] dissipation operator. The [14] dissipation operator presents a thicker

shock wave along all upper surface. The intersection of the shock waves from the upper and lower surfaces at the inlet throat is well captured by both schemes.

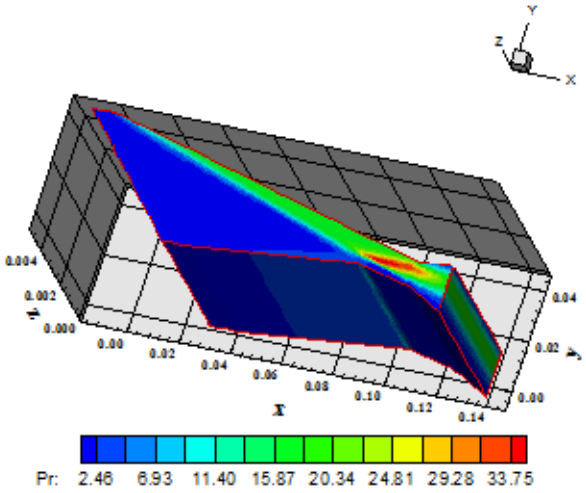

Figure 34. Pressure contours ([2] and [14]).

Figures 35 and 36 present the Mach number contours distributions along the air inlet. In these figures, it is possible to note more pronounced the increase of the thickness of the oblique shock wave along the upper wall captured by the [14] dissipation operator. Moreover, this behavior is also observed at the lower wall. A reason to it can be: due to this operator uses an approximation less correct of the maximum eigenvalue of the Euler equations, the [14] operator distributes more dissipation in the field than it is necessary, whereas the [9] operator, due to a better estimative of the maximum normal eigenvalue of the Euler equations, has a more selective dissipation distribution. In quantitative terms, the Mach number field generated by the [2] scheme and the [9] operator is more intense than that generated by the [14] operator.

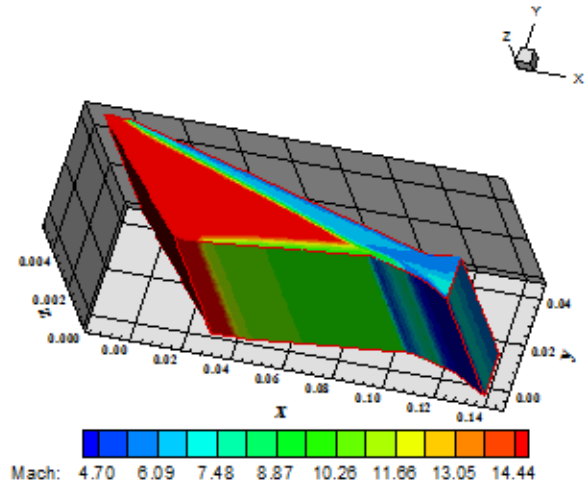

Figure 35. Mach number contours ([2] and [9]).

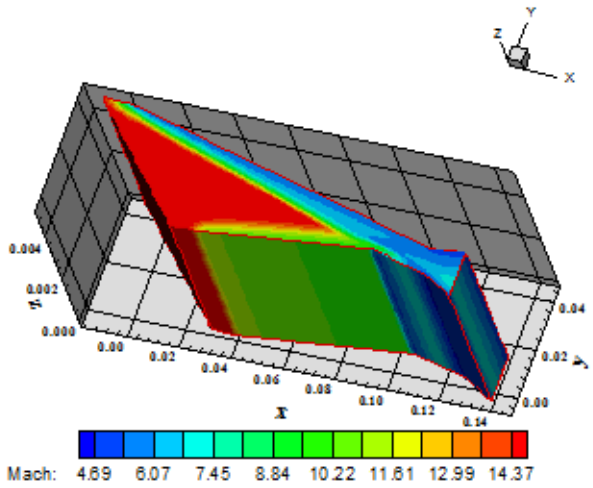

Figure 36. Mach number contours ([2] and [14]).

The robustness of the [2] scheme with [9] and [14] operators is well characterized by the curves of Mach number contours, where the maximum value of this parameter is evidenced. The [2] scheme with [9] operator reached a maximum Mach number of 14.44, whereas the same scheme with operator [14] reached a maximum Mach number of 14.37, a significant difference in CFD.

Figures 37 and 38 exhibit the translational / rotational temperature contours along the air inlet generated by the [2] algorithm using the [9] and [14] artificial dissipation operators, respectively. In this "cold gas" hypersonic flow under study, it is correct to accept the equilibrium between the translational and rotational modes. Even in thermochemical non-equilibrium flows, the hypothesis of equilibrium between these two modes is acceptable; so, there isn't any error in considerate such designation to "cold gas" hypersonic flows. Again, it is possible to verify a thicker oblique shock wave at the air inlet upper surface to the [14] dissipation operator.

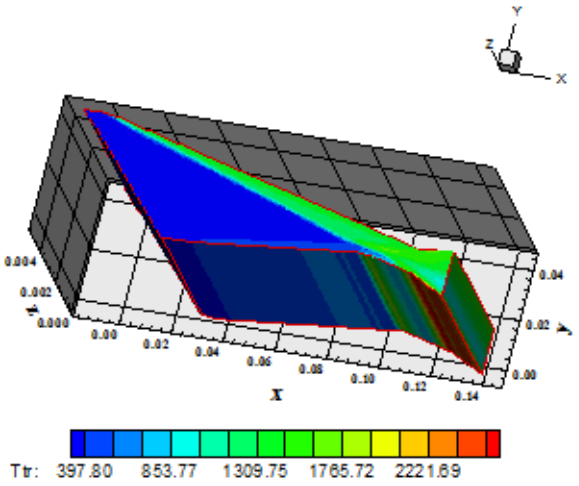

Figure 37. Temperature contours ([2] and [9]).

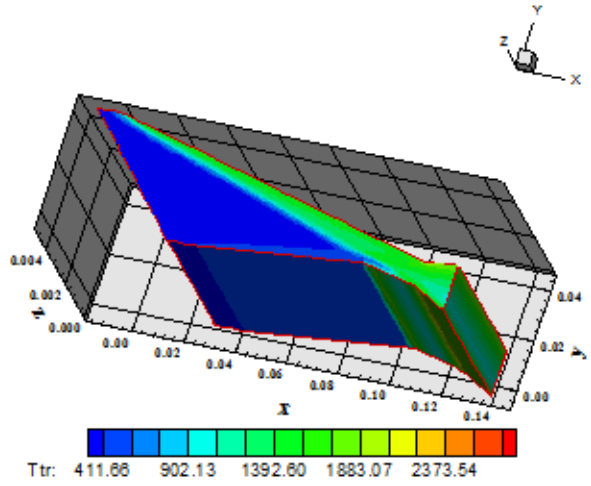

Figure 38. Temperature contours ([2] and [14]).

The [9] dissipation operator allows to the [2] scheme detect a slight variation in the temperature field at the lower surface upstream the throat, as also a bigger heating of the lower surface at the air inlet end region. This ratify the idea of the minor dissipation to the [9] operator than to the [14] operator that, due to the bigger dissipation, eliminate such regions from the solution.

Figure 39 presents the pressure distributions obtained by the [2] scheme using the operators [9] and [14]. As can be seen, there is a meaningful attenuation of the shock plateau at the intermediary region in z (k = KMAX/2). The [2] scheme with the [9] operator still maintain a little of this plateau, but the same scheme using the [14] operator practically eliminates this plateau. The pressure peak, due to the intersection between the lower and upper shock waves, is more intense in the solution obtained with the [9] dissipation operator, as well the pressure recovery at the air inlet end.

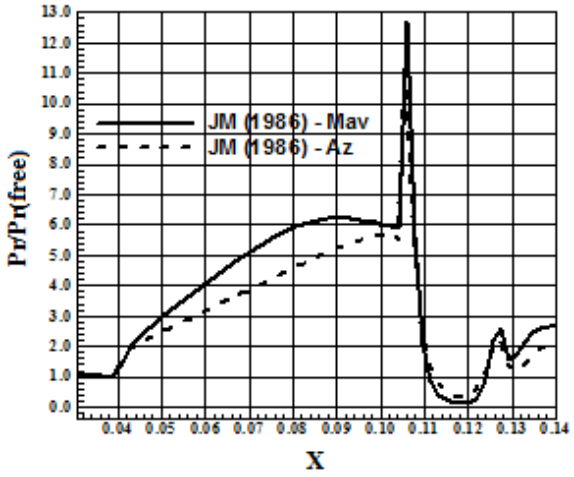

Figure 39. Lower wall pressure distributions.

A parameter which can be analyzed to evaluate the accuracy of the [2] scheme with the two operators is the shock angle of the oblique shock wave that appear at the lower and upper air inlet walls. With a transfer were measured the inclination angles of the lower and upper ramp of the entrance device. To the lower wall this angle was of 6.5° in relation to the horizontal and to the upper wall was of 13.5° in relation to the horizontal. With these angles and with the freestream Mach number was possible to determine the theoretical shock angles of the oblique shock waves. These angles are disposed in Tab. 3, joined with the measured values of them to each operator and the respective percentage error. Figures 33 and 34, at the xy plane, were used to evaluate the measured angles.

Table 3. Measured values of the shock angles of the oblique shock waves.

Surface	Scheme	$\beta^{(Theory)}$	$\beta^{(Measured)}$	Error (%)
Lower	[2]-[9]	10.0	9.0	10.0
	[2]-[14]	10.0	9.6	4.0
Upper	[2]-[9]	17.5	17.5	0.0
	[2]-[14]	17.5	17.2	1.7

As can be seen, the [2] scheme with [14] operator gave the best results considering a global analyses; in other words, the results of the two walls. Although the [9] operator had determined with exact accuracy the value of the shock angle of the oblique shock wave at the air inlet upper wall, its behavior at the lower wall was reasonable, with an error of 10.0%. The [14] operator had errors inferiors to 5.0% in both walls and, therefore, presented the best solution.

8.4 Computational Data

Table 4. Numerical data of the simulations.

Problem	Scheme	CFL	Iterations	Cost[(1)]
VLS	[4]	0.02	7,512	0.0000529
	[6]	0.06	3,473	0.000449
	[2]-[9]	0.30	1,474	0.0001364
	[2]-[14]	0.30	1,735	0.0001227
Diffuser	[4]	0.30	1,212	0.0000529
	[6]	0.70	529	0.000449
	[2]-[9]	1.90	231	0.0001364
	[2]-[14]	2.80	157	0.0001227
Air Inlet	[2]-[9]	0.2	3,735	0.0001364
	[2]-[14]	0.4	2,098	0.0001227

(1) Measured in seconds/per iteration/per cell.

Table 4 presents the numerical data of the VLS, diffuser and air inlet simulations. The computational cost is determined as the simulation time divided by the number of hexahedral cells and by the number of iterations to convergence. As can be seen from this table, the [2] scheme with the [9] dissipation operator is the most expensive, being 203.79% more expensive than the [6] scheme, the cheapest. The solution quality obtained by the [2] scheme using the [9] dissipation operator is what justify its implementation and use.

As final conclusion of this work, the [2] scheme with [9] operator was the best because was more robust, joint with the [14] operator, and generated more accurate solutions. In the VLS problem, this scheme detected with more accuracy the stagnation pressure ahead of the configuration; in the diffuser problem captured with more accuracy the two shock angles of the oblique shock waves; and in the air inlet problem captured with reasonable accuracy the shock angles of the oblique shock waves. In qualitative terms, it was one of the minus dissipative, as exhibited in the air inlet problem. Hence, the [2] scheme with the artificial dissipation operator of [9] is the most recommended to studies of supersonic and "cold gas" hypersonic flows in three-dimensions as employed the algorithms herein analyzed. This scheme provides confinable results and is more robust than the TVD schemes herein studied. Spite of the computational cost, as seen in [9], this scheme justify its use by the solution quality and robustness.

9 Conclusions

The present work compares the numerical methods of [2], [4] and [6], using a finite volume formulation and a structured spatial discretization, applied to the solution of the Euler equations in three-dimensions. All schemes are second order accurate in space. The [2] scheme is also second order accurate in time and uses an artificial dissipation operator to guarantee convergence to the steady state solution. The [4] and [6] schemes are first order accurate in time. The steady state physical problems of the supersonic flow around a simplified configuration of the VLS (Brazilian Satellite Launcher) and the hypersonic flows along a diffuser and along an air inlet are studied. A spatially variable time step procedure is implemented aiming to accelerate the convergence process. This technique has presented excellent gains in terms of convergence ratio, as reported in [7-8].

The results have demonstrated that the [2] scheme, using the [9] dissipation operator, presents the best characteristics of robustness and accuracy.

As final conclusion of this work, the [2] scheme with [9] operator was the best because was more robust, joint with the [14] operator, and generated more accurate solutions. In the VLS problem, this scheme detected with more accuracy the stagnation pressure ahead of the configuration; in the diffuser problem captured with more accuracy the two shock angles of the oblique shock waves; and in the air inlet problem captured with reasonable accuracy the shock angles of the oblique shock waves. In qualitative terms, it was one of the minus dissipative, as exhibited in the air inlet problem. Hence, the [2] scheme with the artificial dissipation operator of [9] is the most recommended to studies of supersonic and "cold gas" hypersonic flows in three-dimensions as employed the algorithms herein analyzed. This scheme provides confinable results and is more robust than the TVD schemes herein studied. Spite of the computational cost, as seen in [9], this scheme justify its use by the solution quality and robustness.

10 Acknowledgments

The present author acknowledges the CNPq by the financial support conceded under the form of a DTI (Industrial Technological Development) scholarship no. 384681/2011-5. He also acknowledges the infra-structure of the ITA that allowed the realization of this work.

References:

[1] R. W. MacCormack, The Effect of Viscosity in Hypervelocity Impact Cratering, *AIAA Paper 69-354*, 1969.

[2] A. Jameson, D. J. Mavriplis, Finite Volume Solution of the Two-Dimensional Euler Equations on a Regular Triangular Mesh, *AIAA Journal*, Vol. 24, No. 4, 1986, pp. 611-618.

[3] A. Jameson, W. Schmidt, E. Turkel, Numerical Solution for the Euler Equations by Finite Volume Methods Using Runge-Kutta Time Stepping Schemes, *AIAA Paper 81-1259*, 1981.

[4] H. C. Yee, R. F. Warming, A. Harten, A High-Resolution Numerical Technique for Inviscid Gas-Dynamic Problems with Weak Solutions, Proceedings of the 8th International Conference on Numerical Methods in Fluid Dynamics, E. Krause, Editor, *Lecture Notes in Physics*, Springer-Verlag, Berlin, Vol. 170, 1982, pp. 546-552.

[5] A. Harten, High Resolution Schemes for Hyperbolic Conservation Laws, *Journal of Computational Physics*, Vol. 49, 1983, pp. 357-393.

[6] H. C. Yee, P. Kutler, Application of Second-Order-Accurate Total Variation Diminishing (TVD) Schemes to the Euler Equations in General Geometries, *NASA-TM-85845*, 1985.

[7] E. S. G. Maciel, Analysis of Convergence Acceleration Techniques Used in Unstructured Algorithms in the Solution of Aeronautical Problems – Part I, *Proceedings of the XVIII International Congress of Mechanical Engineering (XVIII COBEM)*, Ouro Preto, MG, Brazil, 2005.

[8] E. S. G. Maciel, Analysis of Convergence Acceleration Techniques Used in Unstructured Algorithms in the Solution of Aerospace Problems – Part II, *Proceedings of the XVII Brazillian Congress of Engineering and Thermal Sciences (XII ENCIT)*, Belo Horizonte, MG, Brazil, 2008.

[9] D. J. Mavriplis, Accurate Multigrid Solution of the Euler Equations on Unstructured and Adaptive Meshes, *AIAA Journal*, Vol. 28, No. 2, 1990, pp. 213-221.

[10] E. S. G. Maciel, Comparação entre os Algoritmos de MacCormack e de Jameson e Mavriplis na Solução das Equações de Euler e de Navier-Stokes no Espaço Tridimensional, M*ecánica Computacional Journal*, Argentina, Vol. XXIV, No. 12, 2005, pp. 2055-2074.

[11] E. S. G. Maciel, Solutions of the Euler Equations Using Implicit TVD High Resolution Algorithms in Three-Dimensions, *Mecánica Computacional Journal*, Argentina, Vol. XXVIII, No. 18, 2009, pp. 1517-1541.

[12] P. L. Roe, Approximate Riemann Solvers, Parameter Vectors, and Difference Schemes, *Journal of Computational Physics*, Vol. 43, 1981, pp. 357-372.

[13] E. S. G. Maciel, 2009, Explicit and Implicit TVD and ENO High Resolution Algorithms Applied to the Euler and Navier-Stokes Equations in Three-Dimensions – Theory, *Proceedings of the XX International Congress of Mechanical Engineering (XX COBEM)*, Gramado, RS, Brazil.

[14] J. L. F. Azevedo, On the Development of Unstructured Grid Finite Volume Solvers for High Speed Flows, *NT-075-ASE-N*, IAE, CTA, São José dos Campos, SP, Brazil, 1992.

[15] E. S. G. Maciel, Simulação Numérica de Escoamentos Supersônicos e Hipersônicos Utilizando Técnicas de Dinâmica dos Fluidos Computacional, *Doctoral Thesis*, ITA, CTA, São José dos Campos, SP, Brazil, 258p, 2002.

[16] J. D. Anderson Jr., *Fundamentals of Aerodynamics*, McGraw-Hill, Inc., EUA, 563p, 1984.